JOURNAL OF MATERIALS SCIENCE **38** (2003) 2223–2231

Comparison of microstructures for plane shock-loaded and impact crater-related nickel: the microtwin-microband transition

E. V. ESQUIVEL, L. E. MURR, E. A. TRILLO, M. BAQUERA
Department of Metallurgical and Materials Engineering, The University of Texas at El Paso, El Paso, TX 79968-0520, USA

Plane-wave shock-loaded Ni exhibits {111} microtwins which increase in frequency with increasing peak shock pressure above a critical twinning pressure of ~30 GPa. In contrast, microbands coincident with traces of {111} are produced below impact craters in Ni targets by stainless steel projectiles at velocities up to 3.5 km/s. The microband widths are ten times the 0.02 μm twin widths and are characterized by misorientations of roughly 2°. Both shock-loaded and impacted Ni have similar dislocation cell structures which decrease in cell size with increasing pressure or equivalent stress. The exclusive formation of microbands in connection with impact craters in Ni is expected on the basis of its high SFE (~130 mJ/m^2), and a simple dislocation model is developed for the microtwin-microband transition based on graphical summaries which include shock (stress) geometry and SFE effects in FCC metals and alloys. © *2003 Kluwer Academic Publishers*

1. Introduction

Impact crater-related microstructures for polycrystalline copper have exhibited prominent microbands coincident with traces of {111} planes when observed by transmission electron microscopy (TEM) [1, 2]. While microbands have been observed in numerous, severely, quasi-statically and shock deformed metals and alloys, including copper [3–6], shock-deformed copper, particularly plane-wave shocked Cu, had previously exhibited a strong preference for microtwins in the deformation microstructure [7–9]. Sanchez *et al.* [10] have also demonstrated that the oblique shock loading of polycrystalline Cu rods produced intermixed microtwins and microbands; demonstrating that the shock geometry (and correspondingly, the shear stress geometry) might play a key role in the microtwin-microband transition. While the role of stacking-fault (free) energy (SFE) in microband formation in fcc metals and alloys has been unclear [5, 6], recent observations of impact crater-related microstructures for 304 stainless steel [11] and brass (70 Cu-30 Zn) [12] have revealed only a small microband fraction intermixed with microtwins for the stainless steel and only microtwins for the brass. In contrast to Cu with a SFE of roughly 80 mJ/m^2 (at 25°C) [13], stainless steel and brass have SFE's of 20 and 10 mJ/m^2 respectively at 25°C. Consequently, low SFE appears to favor microtwins while high SFE appears to favor microbands, especially where shock-wave geometry or deformation conditions are the same; such as comparisons of residual impact crater-related microstructures.

The present study compares plane-wave, shock-loaded nickel microstructures with impact crater-related microstructures in nickel targets. Nickel is one of the highest SFE fcc metals (~130 mJ/m^2 at 25°C in contrast to 80 mJ/m^2 for Cu [13]) where deformation microtwins have been observed in plane-wave shock loading [9, 14]. Consequently, impact crater microstructures in Ni would be expected to exhibit microbands like Cu [2].

2. Experimental

The details for plane-wave shock loading of polycrystalline nickel sheet and plate (99.9% Ni) have been described in detail elsewhere [9, 14] along with techniques for preparing optical metallographic and TEM specimens [14]. This study examines commercial, polycrystalline Ni (200) sheet having a grain size of 50 μm; shock-loaded at pressures ranging from 30 to 55 GPa; at 2 μs pulse duration [9, 14].

Plates (2.5 cm thick) of commercial Ni (200) (99% Ni) with a grain size of 60 μm were milled to a fine (~20 μm) surface finish and impacted by 3.18 mm diameter stainless (ferritic) steel spheres launched from a light gas gun. Projectile velocities ranged form 0.5 to 3.5 km/s as determined by laser beam occultation and impact flash detectors. Corresponding, instantaneous impact shock (Hugoniot) pressures were calculated from [15]:

$$P_S = \rho_t(C_t + S_t U_{pm})U_{pm} \qquad (1)$$

where ρ_t is the Ni target density (8.9 Mg/m^3), C_t is the bulk sound velocity in the target, S_t is a materials constant related to the Grüneisen parameter [15], and U_{pm} is the modified projectile velocity in the compressed region of the target after impact. The steady-state (Bernoulli) pressure associated with the formed crater is approximated by

$$P_{\mathrm{B}} = \left[\rho_{\mathrm{t}}\rho_{\mathrm{p}} / \left(\rho_{\mathrm{t}}^{1/2} + \rho_{\mathrm{p}}^{1/2}\right)^2\right] u_{\mathrm{o}}^2/2 \qquad (2)$$

where ρ_{t} and ρ_{p} are the Ni target and stainless steel projectile densities (8.9 and 7.9 Mg/m^3 respectively), and u_{o} is the impact velocity. This pressure is correspondingly much less than the Hugoniot shock pressure, especially at higher impact velocities (>2 km/s). For example, at the maximum impact velocity of 3.5 km/s^{-1}, $P_{\mathrm{S}} = 105$ GPa and $P_{\mathrm{B}} = 15$ GPa.

The impact craters were examined as described in previous studies [1, 2, 11, 12] by cutting them into half sections parallel to the impact axis and polishing and etching the half sections with a solution composed of 75 mL HNO_3 to which 10 to 12 drops of HF were added. Specimens for TEM were prepared by cutting thin slices from the half sections, or at other angles, in order to locate microstructure regimes at specific distances from the crater wall. These slices were ground to ~0.2 mm thickness and 3 mm TEM discs punched from them. The TEM discs were electropolished in a solution consisting of in a Tenupol-3, dual-jet electropolishing unit. TEM observations were made in a Hitachi electron microscope operating at 2000 kV; utilizing a goniometer-tilt stage.

3. Results and discussion

Fig. 1 illustrates the grain structure (Fig. 1a), and the grain substructure (Fig. 1b), consisting of large (~1 μm), poorly-formed dislocation cells, for the Ni target plate. These microstructures were also very typical of the starting Ni sheet specimens for plane-wave shock loading as well. The average plate and sheet starting hardness was 0.9 GPa.

Fig. 2a shows an example of shock-induced, deformation microtwins at the critical twinning pressure for Ni of 30 GPa [16] while Fig. 2b illustrates a higher density of microtwins at a higher peak shock pressure of 45 GPa. The intersection of microtwins marked, tw, in Fig. 2b is a typical region of microtwin intersection where the average twin width can be observed to be around 0.02 μm. The orientation or zone axis in both Fig. 2a and b is [001] and in Fig. 2a the remnants of a much smaller dislocation cell structure than the starting cell structure in Fig. 1b can be observed. Prominent twin reflections for microtwins coincident with traces of both [220] and [$2\bar{2}0$] are observed in the selected-area electron diffraction (SAED) pattern insert in Fig. 2b. Average hardnesses for the 30 GPa shocked samples and the 45 GPa shocked samples were 2.2 and 2.5 GPa, respectively.

Fig. 3 shows a typical Ni crater cross-section corresponding to an impact velocity of 3.5 km/s. This produced a peak shock (Hugoniot) pressure at the instant of impact (Equation 1) of 105 GPa and a corresponding Bernoulli pressure (Equation 2) of 15 GPa as noted previously. Spalled stainless steel projectile fragments can be observed in the crater interior in Fig. 3a. Fig. 3b shows linear defects within heavily deformed and distorted grains which occurred in a region roughly 1 mm from the crater wall, along the impact axis as noted in Fig. 3b. These linear microstructures are observed to be microbands as illustrated typically in the TEM images shown reproduced in Fig. 4. Fig. 4a shows microbands in a [112] orientation as the shock-induced microstructure while Fig. 4b shows similar microbands along traces of ($\bar{1}11$) planes at 90° to the (110) grain surface orientation. Note the absence of $\langle 111\rangle/3$ twin reflections in the SAED pattern insert in Fig. 4, and the slight arcing of diffraction spots (arrows) indicative of microband misorientations of roughly 2°. The microband widths in Fig. 4 are also observed to be roughly 0.2 μm in contrast to 0.02 μm measured for the microtwins in Fig. 2b. In Fig. 4b the dislocation walls for the microbands would be perpendicular to the (110) surface if these walls were coincident with the ($\bar{1}11$) planes. In both Fig. 4a and b the microband walls are thick and the microbands themselves evolving from a dense dislocation cell structure similar to the microtwin evolution at a critical plane shock pressure in Fig. 2a. The microband features illustrated in Fig. 4 are characteristic of those noted previously for Cu [2] and stainless steel [11] impact craters. Only microbands similar to those shown in Fig. 4 were observed in the deformed regions below all the impact craters in Ni targets as might be expected in considering its high SFE of 130 mJ/m^2 in contrast to an SFE of 80 mJ/m^2 for Cu where only microbands occur in the deformed regions below impact craters [2].

It is of interest to note that at the Ni crater wall in Fig. 3a there is a narrow (~100 μm) zone of dynamically recrystallized grain structure similar to that observed for all other impact craters in metal or alloy targets [2, 11, 12]. This zone is followed by the microband zone illustrated typically in Fig. 3b, which coincides with a region of maximum residual microhardness of 2.2 GPa. The same features were observed for the occurrence of microbands in Cu [2] while in stainless steel [11] and brass [12], microtwins were observed in this hard zone. Just beyond the microband zone, and intermixed with the microbands very dense dislocation cells are observed (Fig. 4) which become less dense (or larger) with distance from the crater wall. This progression of dislocation cell size increase also coincides with decreasing microhardness into the target until the base microstructure and corresponding base (or starting target) hardness (~0.9 GPa) is reached. This feature is also observed in plane shock loaded Ni where dislocation cells form with increasing density and decreasing dislocation cell size as the peak shock pressure increases up to the critical twinning pressure (~30 GPa [16]) where microtwins emerge in the microstructure as shown in Fig. 2a. This phenomenon is characteristic of microstructural similitude [17], and is illustrated in the comparative microstructures in Fig. 5. The similarities of dislocation cell structures illustrated for plane shock loaded and impact crater-related Ni microstructures in Fig. 5 attests to the similarities in or compensating effects of shock pressure, shear

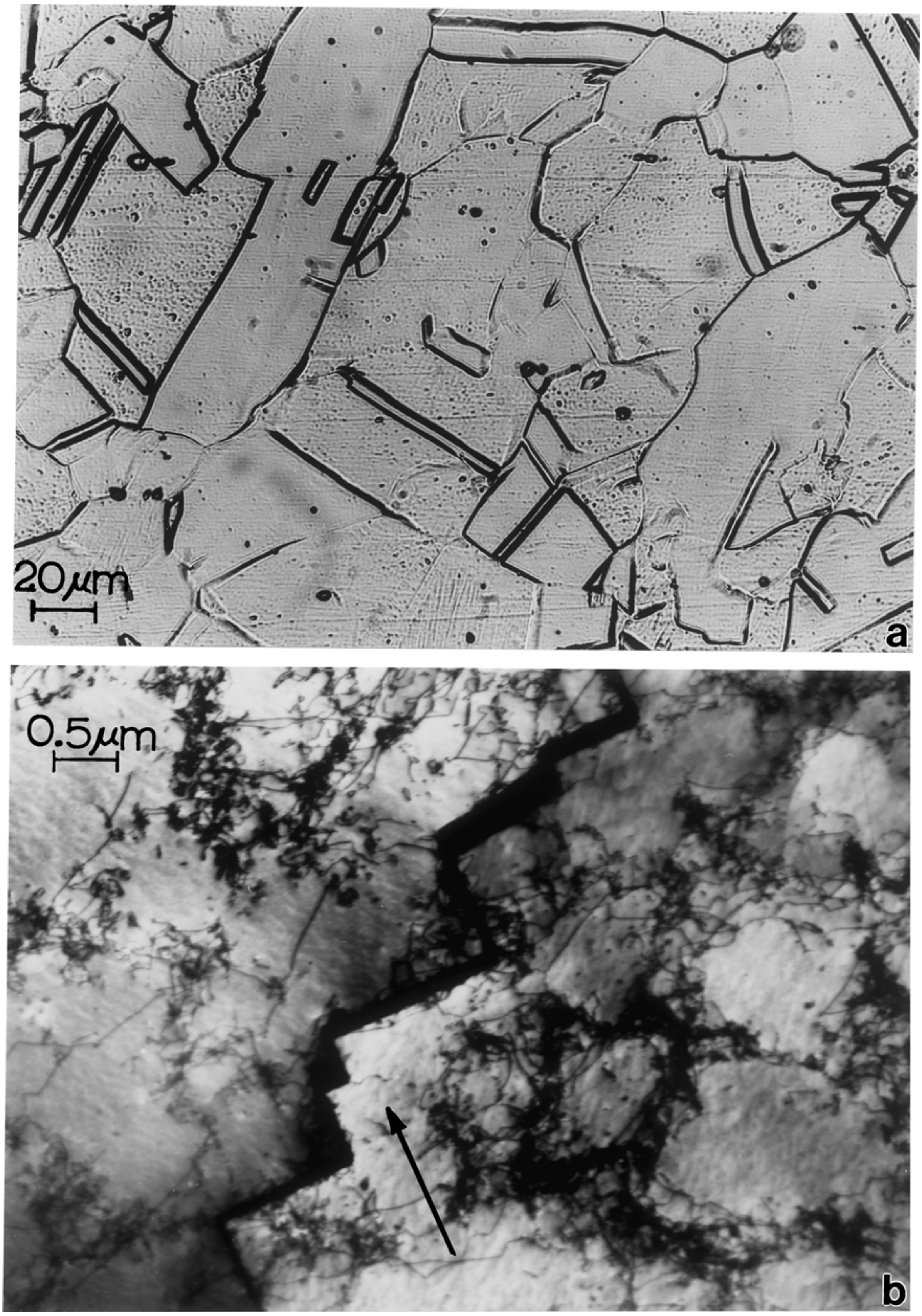

Figure 1 Starting (reference) microstructures for Ni plate. (a) Typical grain structure with annealing twins (straight boundaries). Average grain size of 50 μm. (b) Poorly formed dislocation cell substructure. The grain surface orientation is (112). The arrow denotes the $[1\bar{1}0]$ direction corresponding to the coherent segments of a stepped annealing twin.

stress (shear strain) and shock geometry. However, the dislocation cells in Fig. 5a are only half the cell diameter (center-to-center distance) of Fig. 5b, although the cell walls in Fig. 5b appear to be more dense and thicker than those in the shocked sample in Fig. 5a. Dislocation cell size in Ni has been shown to decrease systematically with increasing peak shock pressure [17, 18] (and with increasing strain) in more conventional deformation [17, 19]. Compare Fig. 5 with Fig. 1b for example where in contrast the hardness essentially

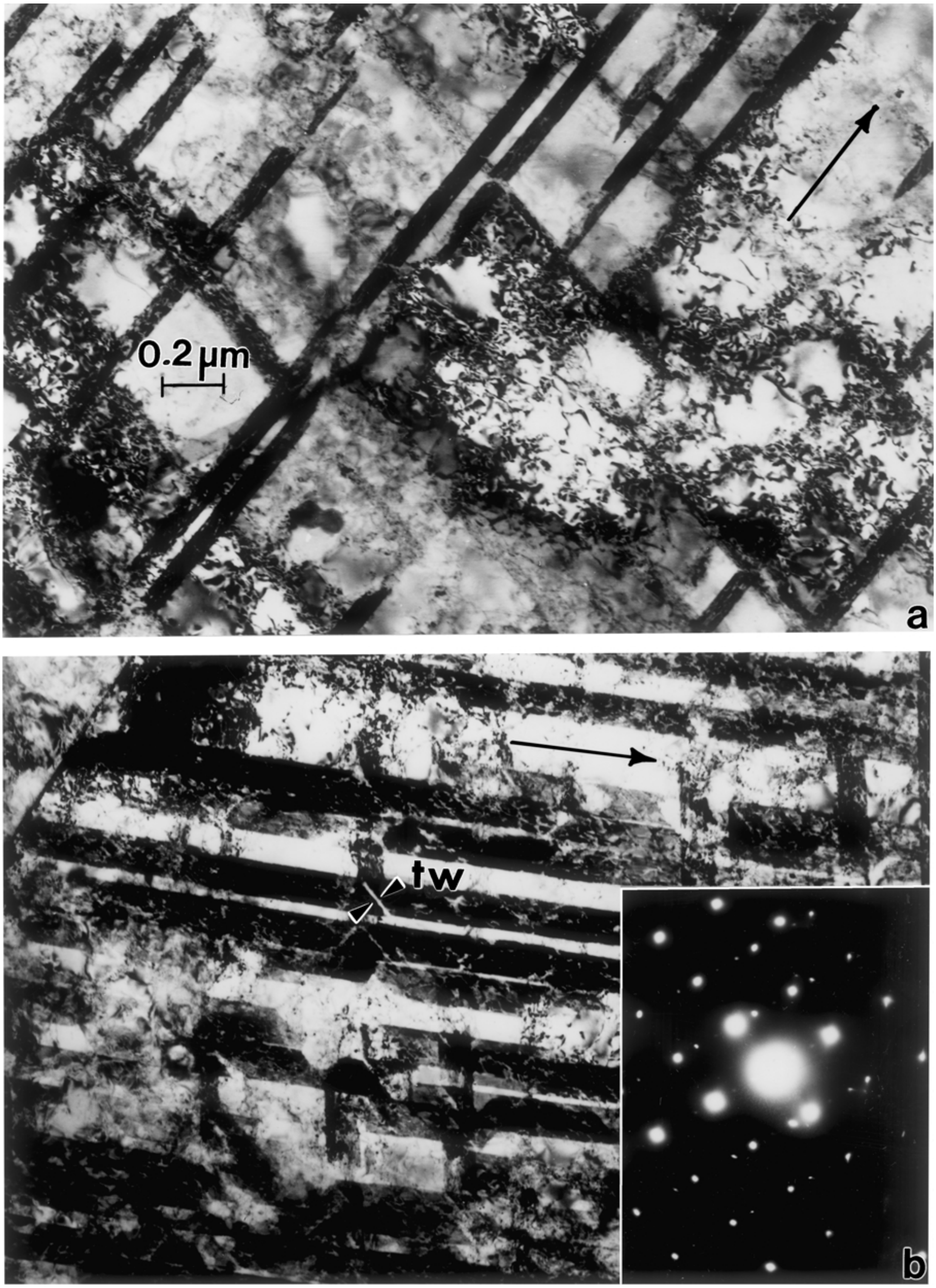

Figure 2 TEM bright-field images of microtwins in plane-wave shock loaded Ni. (a) Peak shock pressure of 30 GPa. [001] zone. (b) Peak shock pressure of 45 GPa. [001] zone. The arrows in (a) and (b) correspond to the [220] direction. Twin reflections are illustrated in the SAED pattern insert in (b). Small arrows marked (tw) show twin intersection volume whose width is characteristic of the microtwin width. The magnifications of (a) and (b) are the same and shown in (a).

doubles while the dislocation cell size is reduced by nearly 1/2. The similarities in dislocation cell structure in Fig. 5 as a transition to either deformation-induced microtwins or microbands suggests some similarities in critical or characteristic shear stress favoring either microtwins or microbands. On the otherhand, the actual formation of microbands or microtwins now appears to involve a correspondence in shock geometry or SFE. That is, when the shock geometry is the same, as in impact cratering, the microtwin-microband transition

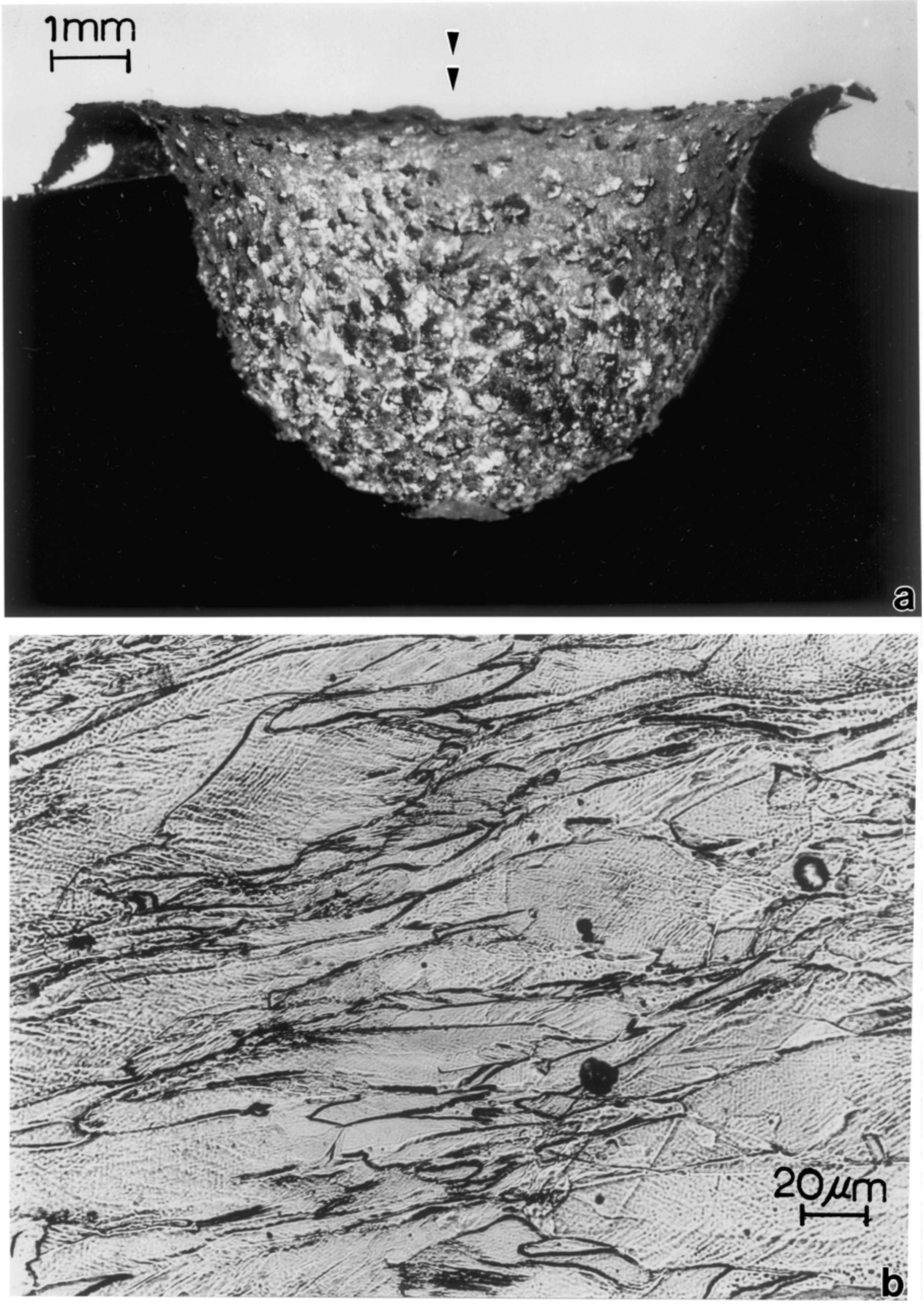

Figure 3 Impact crater half section (a), and corresponding optical metallographic view of typical deformation macrostructure approximately 1 mm from the crater wall; along the impact axis (b). The impact crater corresponds to a Ni target impacted by a stainless steel projectile at 3.5 km/s ($P_S \cong$ 105 GPa).

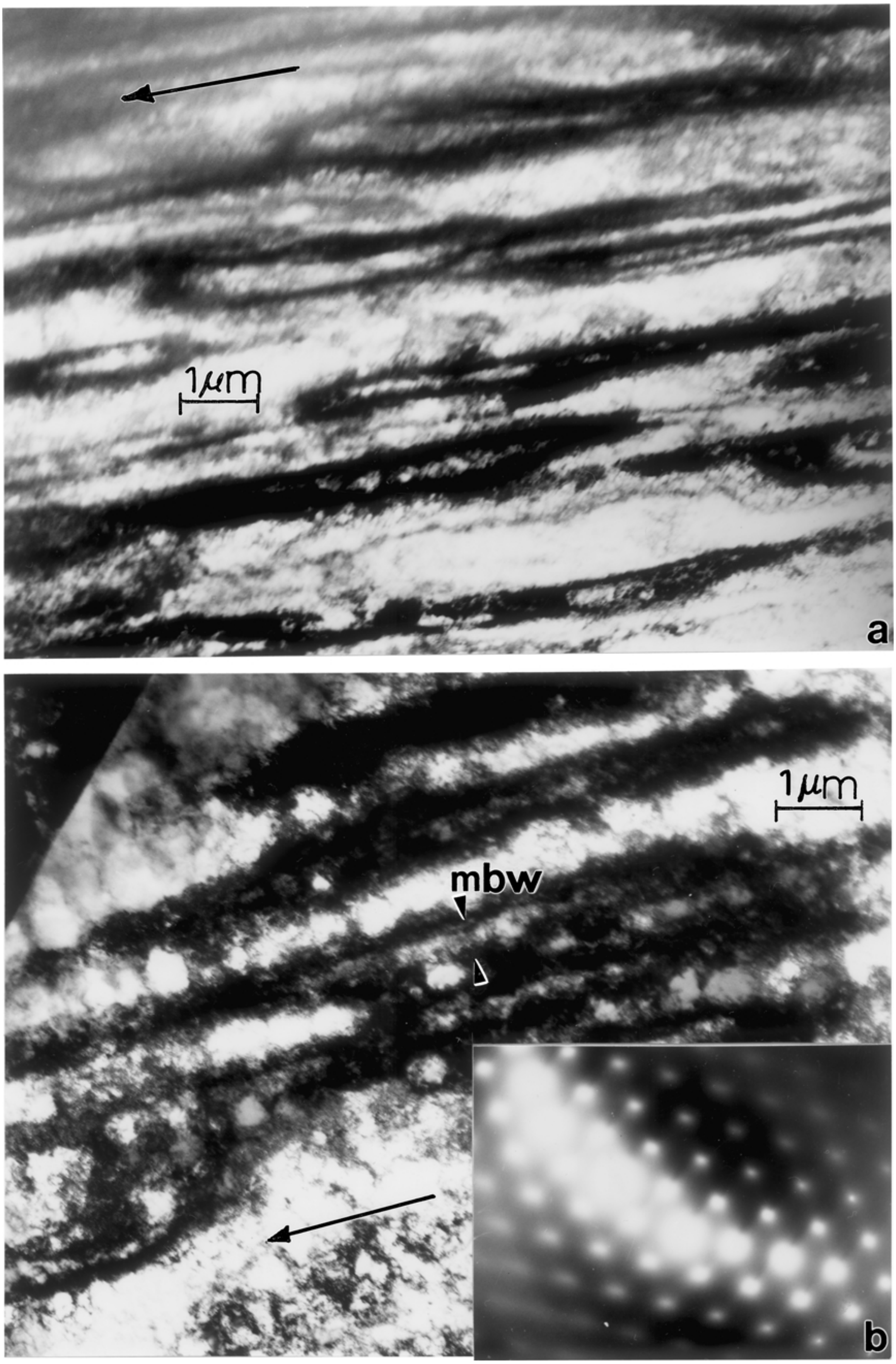

Figure 4 TEM bright-field images of microbands which dominate impact crater microstructures characteristic of Fig. 3b. (a) Microbands in [112] zone. The arrows coincides with the $[13\bar{2}]$ direction. (b) Microbands in [110] zone. SAED pattern insert shows small (∼ 2°) misorientation. No twin spots occur. The large arrow coincides with the $[1\bar{1}2]$ direction. The microband width is denoted (mbw).

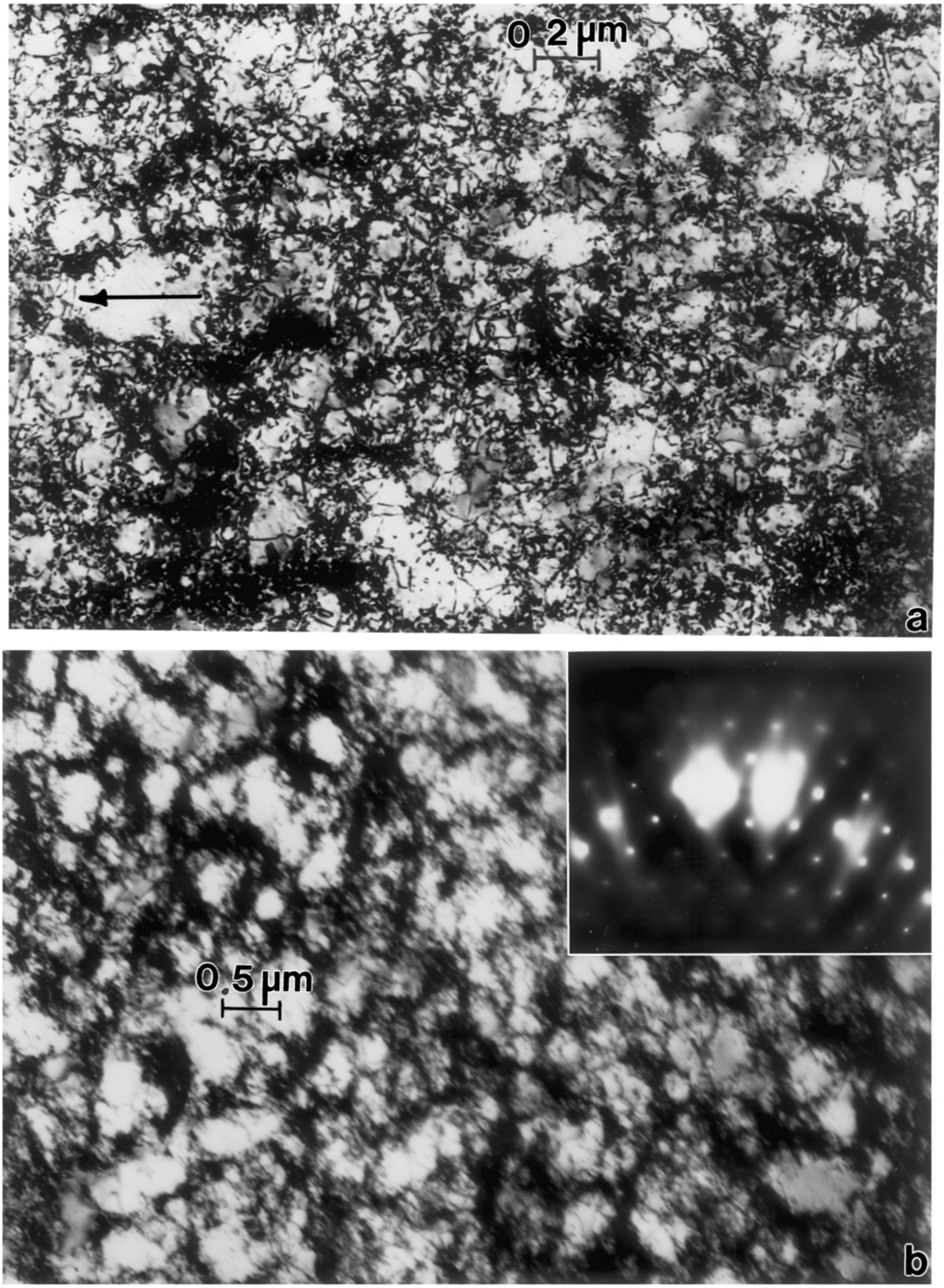

Figure 5 Comparison of similar dislocation cell structures. (a) Ni plane shock loaded at 30 GPa [001] zone. Arrow denotes the [220] direction. (b) Ni substructure located roughly 5 mm from the crater wall in Fig. 3a along the impact axis. SAED pattern insert shows [011] zone. **g** = [200] in (a) and (b).

is clearly SFE dependent: high SFE fcc metals (such as Ni and Cu) produce microbands while low SFE metals or alloys (such as stainless steel and brass) produce microtwins. Correspondingly, for any SFE (fcc) metal or alloy, plane shock produces microtwins at critical twinning pressures which increase with increasing SFE [16] especially where there is essentially no compressive strain component ($\varepsilon_Z \cong 0$) [9].

It is also of interest to note that while plane shock loading usually does not involve any measurable compressive strain ($\varepsilon_Z \sim 0$) [9] in contrast to very high strain associated with impact crater formation, microbands can be formed at some distances from the crater wall, and in regions where there is no recognizable grain distortion as shown in Fig. 3b; corresponding to negligible residual strain. Consequently the contrast between plane and spherical shock (as it applies to impact crater formation and microtwin versus microband microstructures) would seem to be dominated by maximum shear stress geometry rather than shear strain differences.

In plane-wave shock loading, the deviatoric (shear) stresses generated at the (plane) shock front (at 45° to the principal or normal stress) are accommodated by twinning, and the critical shear stress to initiate or nucleate twins is related to the critical twinning (peak) pressure which is SFE dependent: increasing with increasing SFE [16, 18]. This also coincides with the slip-twinning transition stress which is grain size dependent: increasing for decreasing grain size [9]. In general, twinning is focused along the crystallographic orientation in which the resolved shear will tend to decrease the externally applied shear or decrease the overall internal energy. In high SFE fcc metals like Ni, the cooperative movement of dislocations on parallel {111} planes to produce deformation twin-faults or microtwins competes with cross-slip which is favored as SFE increases, and is a dominant feature for Ni where the SFE is high. Correspondingly, the critical pressure for twinning is also high as noted.

In impact loading or point loading to produce an impact crater at Hugoniot shock pressures which are far in excess of the plane-shock critical twinning pressure, the deviatoric (shear) stress varies along the spherical shock front with an expanding radius vector into the target. This produces a strong secondary, non-coplanar shear which results in localized, secondary slip. In effect, the spherical shock geometry suppresses the cooperative, coplanar dislocation glide to produce microtwins especially in high SFE materials where cross-slip is highly favored. Basinski and Mitchell [20] have described the stabilization of primary (slip) dislocations by secondary dislocations on cross-slip planes and Jackson [5] considered cross-slip to be an important issue in microband formation. The model of Huang and Gray [6] for microband formation involves a heterogeneous substructure development closely related to course slip bands lying on the active slip {111} planes in fcc materials; forming an elongated, dislocation double-wall configuration lying in the trace of {111} planes. This involves the generation of polarized dislocations on primary slip system followed by an annihilation process for the primary dislocations in the central portion of slip band structures forming double dislocation walls parallel to the {111} planes, and finally the induction of secondary slip by internal stresses associated with the region between the double walls.

It should also be mentioned that during shock and impact loading a material is subjected to a compression wave followed by a release wave. Consequently the Bauschinger effect (in which prior plastic deformation in the compressive direction can reduce the flow stress in the release wave direction [21, 22]) is apparent and can also affect defect generation and defect storage in the material. The loading geometry (plane or spherical shock) can influence essentially the extent of the Bauschinger effect and resulting post-loaded or residual microstructures, although the exact nature of the influence is unknown.

In describing microband formation in bcc mild steel, Thuillier and Rauch [23] allude to latent slip activation in the {110} slip multiplicity regime as a consequence of alternative strain or strain-state application. In effect, this seems to resemble the imposition of a cross-slip or secondary slip component in fcc systems. Indeed, Huang and Gray [6] concluded that the formation mechanism for microbands may be similar in a variety of fcc and bcc metals and alloys.

The present study demonstrates that twinning in plane-wave shock loaded Ni, which has one of the highest critical twinning pressures of any fcc metal or alloy and a correspondingly high SFE (130 mJ/m^2) is superseded by microband formation in Ni impacted at velocities corresponding to peak shock pressures in excess of the plane-shock critical twinning pressures. This change in shock geometry (from planar to spherical) combined with the superposition of large residual strains connected with impact crater formation is responsible for the microtwin-microband transition. However, this transition is SFE dependent since it becomes less efficient in low SFE alloys such as stainless steel [11] and brass [12].

Fig. 6 is an attempt to summarize the experimental implications of the present investigation, and provide a simple, qualitative, graphical representation

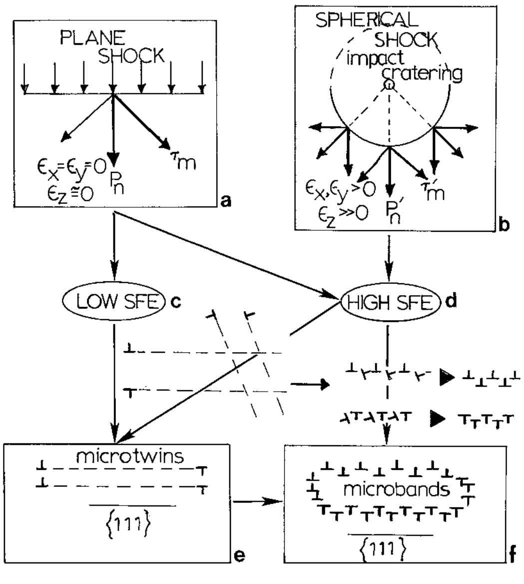

Figure 6 Schematic comparisons for microtwins versus microbands. Microtwins occur almost exclusively in plane shock: a, c + d, e while for high SFE systems microbands occur almost exclusively in impact cratering: b, d, f. Some mixing of microtwins and microbands occurs for intermediate-to-low SFE and for oblique shock/intermediate shock geometries. In plane shock primary dislocation glide produces irregular twin-faults/microtwins. In impact cratering secondary glide/cross-slip creates elongated dislocation wall structures coincident with {111}. P_n denotes the normal pressure while T_m is the deviatoric (shear) stress. Note in impact cratering the coincidence of P_n' and T_m' at radius vector angles of 45° and 90°.

for the microtwin-microband transition in fcc metals and alloys. The principal features of Fig. 6 include a representation of the planar shock versus impact crater/spherical shock geometries, primary and secondary slip (or cross-slip), primary-secondary dislocation interactions to form a stable dislocation wall structure, and the corresponding microtwin-microband transition which is also strongly influenced by SFE, especially extremes in SFE, i.e., brass at 10 mJ/m^2 versus Cu at 80 mJ/m^2, for example. The graphics in Fig. 6 show that when a secondary slip system is imposed on the primary dislocation motion on parallel $\{111\}$ planes, twinning defers to microband formation especially at higher SFE. However, twinning dominates when the SFE is very low.

4. Conclusions

A comparison of plane-wave shock-induced deformation microtwins in Ni and microbands associated with the deformation regimes proximate to the crater walls in impact craters in Ni target plates seems to confirm the effect of shock geometry (plane versus spherical) on the microtwin-microband transition. This variation in microtwins versus microbands as a consequence of deformation mode change was expected on the basis of SFE influencing the transition since identical results were observed earlier for Cu which also possesses a high SFE ($\sim$80 mJ/m^2) but not as high as Ni ($\sim$130 mJ/m^2). The microbands are roughly 10 times the microtwin widths and microband misorientations are $\sim 2^\circ$. These observations are completely consistent with observations previously made in Cu [10].

Acknowledgments

This research was supported by a NASA MURED Grant NAG-9-1171 and NASA Grant NAG-9-1100 through the NASA Johnson Space Center, Houston, TX. We are grateful to Dr. Fred Hörz (NASA-Houston) for developing the craters in the nickel target plate. Andy Bujanda also helped with aspects of measuring and characterizing the experimental craters and is gratefully acknowledged.

References

1. S. A. QUINONES, J. M. RIVAS and L. E. MURR, *J. Mater. Sci. Lett.* **14** (1995) 685.
2. S. A. QUINONES and L. E. MURR, *Phys. Stat. Sol.* (a) **166** (1998) 763.
3. M. HATHERLY and A. S. MALIN, *Metal Tech.* **6** (1979) 308.
4. A. S. MALINE and M. HATHERLY, *ibid.* **13** (1979) 463.
5. P. J. JACKSON, *Scripta Metall.* **17** (1983) 199.
6. J. C. HUANG and G. T. GRAY III, *Acta Metall.* **37**(2) (1989) 3335.
7. R. J. DEANGELIS and J. B. COHEN, *J. Metals* **15** (1963) 681.
8. F. I. GRACE, *J. Appl. Phys.* **40** (1969) 2649.
9. L. E. MURR, in "Shock Wave and High-Strain-Rate Phenomena in Metals," edited by M. A. Meyers and L. E. Murr (Plenum Press, New York, 1981) Chap. 37, p. 607.
10. J. C. SANCHEZ, L. E. MURR and K. P. STAUDHAMMER, *Acta Mater.* **45**(8) (1997) 3223.
11. L. E. MURR, E. A. TRILLO, A. A. BUJANDA and N. E. MARTINEZ, *ibid.* **50** (2002) 121.
12. B. GONZALES, L. E. MURR, O. L. VALERIO, E. V. ESQUIVEL and H. LOPEZ, *Mater. Characterization*, in press.
13. L. E. MURR, "Interfacial Phenomena in Metals and Alloys" (Addison-Wesley, Reading, MA, 1975); reprinted by Tech Books, Herndon, VA, 1991 and available from CBLS, 119 Brentwood St., Marietta, OH 45750; FAX: 740-374-8029.
14. F. GREULICH and L. E. MURR, *Mater. Sci. Engng.* **37** (1979) 81.
15. M. A. MEYERS, "Dynamic Behavior of Materials" (Wiley, New York, 1994).
16. L. E. MURR, in "Shock Waves in Condensed Matter" edited by S. C. Schmidt and N. C. Holmes (Elsevier Science, B.V., Amsterdam, 1998) p. 315.
17. L. E. MURR and D. KUHLMANN-WILSDORF, *Acta Metll.* **26** (1978) 847.
18. L. E. MURR, in "Materials at High Strain Rates," edited by T. Z. Blazynski (Elsevier Science, New York/London, 1987) Chap. 1, p. 1.
19. L. E. MURR and S.-H. WANG, *Res. Mechanica* **4** (1982) 237.
20. Z. S. BASINSKI and T. E. MITCHELL, *Phil. Mag.* **13** (1966) 103.
21. C.-C. LI, J. D. FLASCK, J. A. YAKER and W. C. LESLIE, *Met. Trans.* A **9A** (1978) 85.
22. B. SCHOLTES, O. VÖHRINGER and E. MACHERASCH, in Proc. ICMA6 (Pergamon, New York, 1982) Vol. 1, p. 255.
23. S. THUILLIER and E. F. RAUCH, *Acta Metall, et Mater.* **42**(6) (1994) 1973.

Received 20 August 2002
and accepted 26 February 2003